Journal of Materials Chemistry A

ROYAL SOCIETY OF CHEMISTRY

PAPER

View Article Online
View Journal | View Issue

Cite this: J. Mater. Chem. A, 2024, 12, 18127

Advancing anode-less lithium metal batteries: ZnF_2 modification and *in situ* structural regulation for enhanced performance†

Jing Tao,[a] Can Zhang,[a] Xueyang Li,[a] Xinlong Chen,[a] Chenzhen Ji,[b] Wang Wan*[a] and Chao Wang *[a]

Lithium metal anodes tend to form non-uniform Li deposition that causes dendrite growth during cycling. Meanwhile, the deposition and dissolution of lithium metal often results in the continuous formation and breakdown of the SEI. Additionally, the use of thick lithium metal often results in an excessive inventory of lithium, which diminishes the energy advantage of lithium metal. Fabricating thin lithium foils is challenging owing to the low mechanical strength of lithium metal. To address these issues, we employed an *in situ* structural regulation strategy to prepare high-performance lithium metal batteries. The mechanical strength of the prepared LiF@LiZn10/Li foil was significantly enhanced, allowing it to be thinned down to a thickness of 5 μm, accompanied with great air stability. Moreover, the *in situ* formation of LiZn alloys improved Li-deposition behavior. Furthermore, we demonstrated the participation of LiF particles in the *in situ* formation of the SEI, which facilitated Li^+-transport kinetics. The LiF@LiZn10/Li electrode demonstrated significantly enhanced cycling performance by synergistically improving Li-deposition behavior and optimizing the SEI layer *in situ*. The LiF@LiZn10/Li foil electrode exhibited a long cycling life of over 1300 h at 1 mA cm^{-2} and 1 mA h cm^{-2}. When coupled with a commercial $LiFePO_4$ cathode (3.3 mA h cm^{-2}), the $LiFePO_4$||LiF@LiZn10/Li cell exhibited a cycle life approximately thrice that of the cells with LMBs. This work provides a novel strategy to optimize LMAs for next-generation LMBs.

Received 9th April 2024
Accepted 10th June 2024

DOI: 10.1039/d4ta02431a

rsc.li/materials-a

Introduction

The increasing demand for high-energy-density batteries has revitalized interest in lithium metal anodes (LMAs). Possessing an ultrahigh theoretical specific capacity of 3860 mA h g^{-1}, low density of 0.59 g cm^{-3}, and the most negative electrochemical potential (−3.04 V *vs.* the SHE), lithium metal has emerged as an attractive solution for advanced battery technologies.[1,2] However, the practical application of lithium metal anodes faces several challenges. Unlike the graphite anode based on the Li^+-insertion mechanism, the lithium metal anode can achieve a direct Li deposition and lithium dissolution process.[3,4] However, this process encounters numerous challenges, including the uncontrollable growth of lithium dendrites, significant volume change,[5] and the continuous formation of solid-electrolyte interface (SEI) layers.[6,7] These issues can lead to various complications, such as short circuits, the formation of dead lithium, pulverization, and low coulombic efficiency.[8,9] Consequently, these factors result in irreversible capacity loss and decreased cycle life, and in severe cases, they can even cause safety issues such as fires and explosions.[10,11] Overall, these challenges severely hinder the development of lithium metal batteries.

The behavior of Li deposition is largely influenced by lithium nucleation and Li^+ transport within lithium anode materials.[12] Lithium dendrite formation and growth primarily result from random Li^+ nucleation sites and uneven distribution of local current density.[13] To address this challenge, establishing uniform nucleation sites using lithiophilic materials can promote uniform nucleation and facilitate homogeneous Li deposition, thereby significantly reducing the nucleation overpotential of the lithium electrode.[14,15]

Introducing appropriate Li-metal alloys with good lithium affinity and wetting properties can effectively provide uniform and abundant deposition sites, preventing the growth of dendrites during electrochemical cycling processes. Zn as a material with good lithium affinity and wetting properties can effectively provide uniform and abundant deposition sites, preventing the growth of dendrites during electrochemical cycling processes.[16–19] Additionally, the uniform dispersion of nanoscale LiAl alloys within the matrix is beneficial for

[a]School of Materials Science and Engineering, Tongji University, Shanghai 201804, China. E-mail: chaow@tongji.edu.cn; 21310104@tongji.edu.cn
[b]School of Mechanical Engineering, Tongji University, Jiading District, Shanghai 201804, China

† Electronic supplementary information (ESI) available. See DOI: https://doi.org/10.1039/d4ta02431a

inducing the uniform deposition of metallic lithium and effectively suppressing side reactions.[20] LiSn alloys also have a lower nucleation barrier for lithium and exhibit great lithiophilicity, which can regulate the deposition and stripping behavior of Li^+.[15,21] The direct incorporation of alloying elements into molten lithium facilitates the formation of *in situ* Li–M alloy frameworks,[22] serving as mixed ions and electron conductors (MIECs).[23,24]

The inherent reactivity and significant volume changes observed during the cycling of lithium metal often result in the continuous formation and breakdown of the SEI, leading to the consumption of active lithium materials and electrolytes.[25] This phenomenon not only contributes to a notable reduction in coulombic efficiency but may also lead to electrode pulverization.[26,27] To address these challenges, researchers have explored methods to enhance the stability and mechanical integrity of the SEI layer. Incorporating lithium fluoride (LiF) into the SEI has been shown to improve its chemical stability and mechanical strength, thereby facilitating a stable interface between LMAs and corrosive solvent molecules.[28] Optimizing the formation of a LiF-rich SEI can be achieved through the utilization of fluorinated solvents, additives, and negative electrodes containing fluorine.[29,30]

Furthermore, many lithium metal batteries (LMBs) investigated in previous studies utilized thick lithium foil exceeding 300 μm as the anode, leading to a significant excess of lithium that diminished the energy advantage of using lithium metal as the anode. For instance, employing a 300 μm-thick lithium metal anode (equivalent to an areal capacity of 60 mA h cm^{-2}) alongside a commercial cathode with a capacity of 3 mA h cm^{-2}, the energy density achieved by using lithium as the anode was lower than that obtained with graphite, and with considerably poorer cycling stability.[31] Taking a pragmatic approach, it is evident that only the utilization of thin lithium metal anodes, typically less than 50 μm, can yield advantages for high-energy-density batteries.[32]

However, it is challenging to fabricate thin lithium foils due to the low mechanical strength of lithium metal.[33] To address this limitation, researchers have begun to explore lithium alloys to enhance the machinability of lithium metal for preparing ultrathin lithium foils. By incorporating silver into lithium metal to form LiAg alloys, the machinability of lithium metal can be greatly improved, enabling the fabrication of ultrathin lithium foils.[34,35] By utilizing the lithiophilicity of LiZn alloys, the molten LiZn alloys can be easily spread on a copper foil and form a controllable thickness negative electrode.[18] Additionally, LiSn alloys enable the large-scale printing of flexible ultrathin (15 μm) lithium alloy negative electrodes.[36]

When designing and optimizing LMAs, one of the primary considerations is the use of lithiophilic elements. Among the lithiophilic materials, lithium alloying materials have attracted significant attention, as they offer not only enhanced mechanical properties but can also improve the deposition behavior of lithium. Here, we evaluated a range of alloying materials based on their lithiophilic degree, cost, deposition behavior, volume stability, and other factors to identify suitable materials. Furthermore, the formation of a LiF-rich SEI has been found to be highly beneficial for LMAs.[37] Taking inspiration from this, our experiments further introduced LiF particles, which contribute to the formation of an SEI rich in LiF based on introducing lithiophilic elements. In this study, we introduced metal fluorides (MF_n) into lithium. Metal fluorides react with molten lithium to produce LiF particles and LiM alloys, typically $n \geq 2$. The reactions are demonstrated as follows:

$$Li + MF_n \rightarrow nLiF + Li \quad (1)$$

$$Li + M \rightarrow LiM \quad (2)$$

Consequently, we could create a uniform Li-alloy foil with enhanced mechanical strength, facilitating the fabrication of thin Li-alloy foils. The introduction of the alloy modulates the Li-deposition behavior, whereby the LiF-rich foil can gradually release LiF, thereby *in situ* regulating the SEI during cycling. This could effectively improve the electrochemical deposition behavior of Li^+ on the lithium metal surface, enhance the stability of the electrode, and improve the electrochemical performance. In the process of optimizing the LMAs, we not only synergistically improved the deposition behavior of lithium from multiple aspects but also achieved the *in situ* control of the SEI during electrochemical cycling. This *in situ* structural regulation strategy offers a novel approach to simultaneously address dendrite formation and interface design for lithium composite anodes.

Through a series of systematic experiments aimed at optimizing the elemental composition and concentration, we identified that 10 wt% ZnF_2 was the optimal additive concentration. The resulting composite anode, denoted as LiF@LiZn10/Li, offered several advantages. Leveraging a LiF-rich interface and LiZn-strengthened bulk, the LiF@LiZn10/Li foil enabled the fabrication of composite anodes with thicknesses ranging from 5 to 50 μm *via* roll-to-roll pressing. Additionally, it exhibited superior air resistance, enduring 144 h in a 20% relative humidity environment. Furthermore, it could effectively modify the deposition behavior, leading to long-term cycling stability, surpassing 1300 h in symmetrical cells under 1 mA cm^{-2} and 1 mA h cm^{-2}. The $LiFePO_4$‖LiF@LiZn10/Li cell exhibited a cycling life approximately three times that of cells with LMBs. A pouch cell featuring an NCM811 cathode and LiF@LiZn10/Li composite anode achieved excellent electrochemical performance with a specific energy of 350 W h kg^{-1}.

Experimental

Material preparation

Different metal fluorides, such as ZnF_2 (Aladdin, 99%), MgF_2 (Aladdin, 98%), SnF_2 (Aladdin, 99%), and SbF_3 (Tansoole, 99%) were mixed with lithium metal to form different composite foil materials. The preparation process of the composite negative electrode material is shown in Fig. 1a. First, high-purity lithium metal (China Energy Lithium Industry Co., Ltd.) was mixed with different metal fluorides through static pressing. Then, the mixtures were placed in a stainless steel container and heated to 250 °C in a glove box while maintaining the H_2O and O_2 content

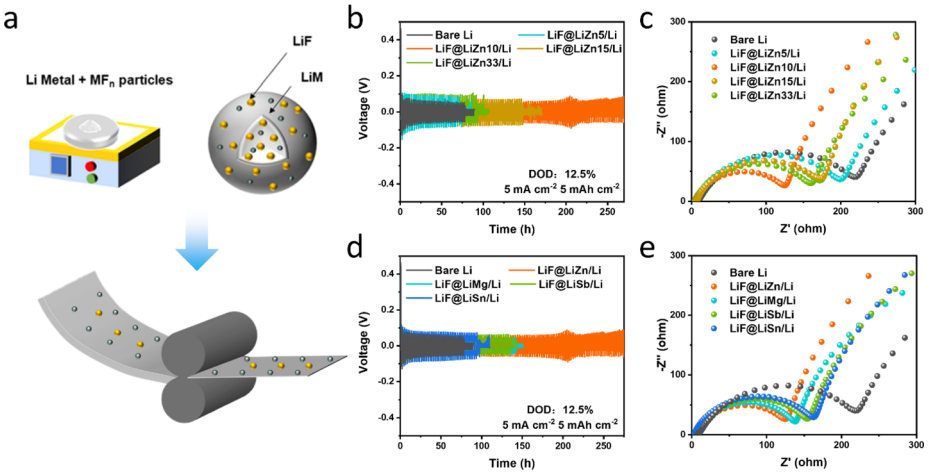

Fig. 1 (a) Process diagram of the LiF@LiM/Li foils. (b) Cycling performance of bare Li and LiF@LiM/Li (M = Zn, Mg, Sb, and Sn) symmetric cells at 5 mA cm^{-2} and 5 mA h cm^{-2}. (c) Nyquist plots of the LiF@LiM/Li (M = Zn, Mg, Sb, and Sn) foil electrodes in symmetric cells. (d) Cycling performance of bare Li and LiF@LiZn/Li symmetric cells with different mass ratios (5%, 10%, 15%, and 33%) at 5 mA cm^{-2} and 5 mA h cm^{-2}. (e) Nyquist plots of the LiF@LiZn/Li symmetric cells with different mass ratios (5%, 10%, 15%, and 33%).

at less than 0.01 ppm. Continuous stirring was employed to ensure thorough mixing and reaction, resulting in the formation of homogeneous composite anode materials. After cooling to room temperature, the resulting composite materials were repeatedly rolled to prepare LiF@LiM/Li foils in a dry chamber with a relative humidity (RH) of 5%.

For the symmetrical cells, we utilized LiF@LiM/Li electrodes and bare lithium electrodes with a diameter of 6 mm and a thickness of 200 μm. In full cells, circular pieces with a diameter of 12 mm were used for both the cathodes and anodes. The cathodes consisted of $LiFePO_4$ cathodes (China Shoto Ltd.) with a loading of 3.3 mA h cm^{-2} (20.6 mg cm^{-2}). The cathodes consisted of NCM811 cathodes (caned) with a loading of 2.8 mA h cm^{-2} (15 mg cm^{-2}). The anode included 50 μm-thick LiF@LiZn10/Li foil anodes and 50 μm-thick bare Li anodes. For the pouch cell, the NCM811 cathode had a size of 5 × 5 cm^2, and 40 μm-thick LiF@LiZn/Li foil anodes were employed.

Electrochemical measurements

The electrochemical performance was measured by a Neware battery test system (CT-4008, Neware) at a temperature of 298 K.

For the symmetric cells, the current density was set at 1 mA cm^{-2} or 3 mA cm^{-2}, with an areal capacity of 1 mA h cm^{-2} or 3 mA h cm^{-2} in an ether electrolyte (1 M LiTFSI DME : DOL = 1 : 1 with 2% $LiNO_3$) and a carbonate ester electrolyte (1 M $LiPF_6$ in DMC : EC = 7 : 3 with 2% VC).

For the full cells, the current density was maintained at 0.5C in the coin cells and 0.1C in the pouch cells. The cells were operated using a carbonate ester electrolyte. The potential range was 2.5–3.7 V for $LiFePO_4$ and 2.8–4.3 V for NCM811.

Electrochemical impedance spectroscopy (EIS) and linear sweep voltammetry (LSV) were performed using a Gamry system. Nyquist plots of symmetric cells were obtained by EIS testing in the frequency range of 1 MHz to 0.1 Hz. Tafel plots for symmetrical cells were acquired by LSV testing in the voltage range of −0.2 V to 0.2 V at a scanning rate of 1 mV s^{-1}.

Characterization

X-Ray Diffraction (XRD) measurements were performed using a Bruker D8-Advance power X-ray diffractometer with Cu Kα radiation (λ = 0.15405 nm). X-Ray Photoelectron Spectroscopy (XPS) analysis was performed on an American Thermo Fisher Scientific ESCALAB 250 Xi. To examine the morphology and structure of the samples, scanning electron microscopy (SEM) images and energy-dispersive X-ray spectrometry (EDS) mapping were performed by field emission scanning electron microscopy (SEM, FEI Quanta 250FEG) under an accelerated voltage of 5 kV. Tensile strength measurements were carried out in a dry chamber with a relative humidity (RH) of 5%.

Results and discussion

Symmetric cells were first fabricated to assess the cycling performance of the prepared LiF@LiM/Li composites, and the results are compared in Fig. 1b. Under cycling conditions of 5 mA cm^{-2} and 5 mA h cm^{-2}, the cycle life of the LiF@LiM/Li composite electrodes demonstrated remarkable improvements compared to the bare Li electrodes, which typically survive for approximately 70 h. Specifically, the cycle life for LiF@LiSn/Li was extended to 125 h, LiF@LiSb/Li to 150 h, LiF@LiMg/Li to 150 h, and LiF@LiZn/Li even more, significantly outperforming the others and lasting for 270 h. The incorporation of MF_n particles significantly enhanced the cycling stability of the Li anode, also indicating that the LiF@LiZn/Li foil can regulate the deposition behavior during the cycling process to exhibit a longer cycle life. Furthermore, as illustrated in Fig. 1c, owing to the modification of the Li/electrolyte interface through the LiM alloys and LiF particles, the interface impedances of LiF@LiM/Li electrodes were notably reduced, with the most

substantial reduction observed in the case of LiF@LiZn/Li electrode. This indicates that the LiF@LiZn/Li foil had better Li^+-transport ability, could form a high-performance SEI film during the cycling process, and enabled a reduced internal impedance of the cell. Based on these electrochemical properties, ZnF_2 was selected as the primary material for optimizing the lithium metal electrodes. Moreover, the cost-effectiveness of zinc also renders it a promising material for future industrial applications.

Further, to explore the influence of different ZnF_2 additions on the electrochemical performance, the cycling performance of LiF@LiZn/Li electrodes with varying addition of ZnF_2 (samples denoted as LiF@LiZn5/Li, LiF@LiZn10/Li, LiF@LiZn15/Li, LiF@LiZn33/Li; where the numbers represent the mass ratio of ZnF_2) was investigated. As Fig. 1d presents, LiF@LiZn5/Li exhibited a similar cycling performance to that of Li metal, suggesting the limited regulation effect from the LiZn alloys and LiF particles from the 5 wt% ZnF_2 addition. Notably, LiF@LiZn10/Li, with a moderate ZnF_2 addition demonstrated the longest cycle life of 270 h. However, with further increases in ZnF_2 addition, the cycling lives of LiF@LiZn15/Li and LiF@LiZn33/Li were reduced to 150 h and 80 h, respectively. The interface impedance results exhibited a similar trend to the cycling performance, as shown in Fig. 1e, and followed the order: Li > LiF@LiZn5/Li > LiF@LiZn15/Li > LiF@LiZn33/Li > LiF@LiZn10/Li. Consequently, LiF@LiZn10/Li, with exceptional cycling stability and minimal impedance, was selected for further in-depth investigation.

It is well-recognized that the machinability of pure lithium metal is difficult. The mechanical strength of lithium is poor, which causes it to crack during rolling, especially when its thickness is decreased down to 50 μm. Meanwhile, lithium can react with Cr_2O_3 on the roller surface, making it stick to the stainless steel roller, and thus, the thinning of Li is troublesome, as shown in Fig. S1.†[32] Fortunately, the formation of LiZn alloys and LiF can dramatically change the mechanical properties of Li metal. As illustrated in Fig. 2a, the LiF@LiZn10/Li foil exhibited a substantially improved tensile strength of approximately 1750 kPa, which was roughly three times that of the bare Li foil of approximately 650 kPa. The elongation at the break of LiF@LiZn10/Li (8%) was also higher than that of pure Li metal (4.5%). When the LiZn alloys and LiF particles are uniformly dispersed in the lithium matrix as finely distributed particles, they interact with dislocations, impeding their movement and increasing the deformation resistance of the alloys. Moreover, the dispersion of LiF particles and LiZn alloys on the surface of the LiF@LiZn10/Li foil acts as a contact inhibitor, which reduces the bonding between the roller and the LiF@LiZn10/Li foil. Benefiting from the enhanced mechanical strength and lowered stickiness, the prepared LiF@LiZn10/Li could be fabricated into large-area foils with ultrathin thicknesses (from 50 μm to 5 μm, as displayed in Fig. S2 and S3†) by a handy rolling procedure. The cross-section SEM images in Fig. 2b and S4† show that the 5 μm-thick and 50 μm-thick LiF@LiZn10/Li foils demonstrated dense structures without holes in the matrix. Additionally, the thinned LiF@LiZn10/Li foil still maintained enough strength. As shown in Fig. S5,† the ultrathin LiF@LiZn10/Li foil could tolerate repeated crimping, bending, and stretching operations without any cracks or tape breaks, which could facilitate the electrode fabrication process in practical applications. Also, the controlled thickness of the LiF@LiZn10/Li foil could support the construction of high-energy density Li metal batteries with a limited N/P ratio.

XRD was performed to explore the phase composition of the LiF@LiZn10/Li foil. The results are shown in Fig. 2c. Peaks corresponding to the intermetallic LiZn alloys were significantly observed at 24.71°, 40.99°, and 65.19°. The peaks of LiF, appearing at 38.7°, 44.99°, and 65.49°, demonstrated a weaker intensity. The EDS mapping in Fig. 2d–f suggested that these particles were LiZn alloys and LiF particles, which were uniformly dispersed on the surface of the LiF@LiZn10/Li. The cross-section image in Fig. S6† further indicated that LiZn and LiF were formed throughout the whole matrix. Furthermore, the distribution of LiZn alloys and LiF particles in the matrix also appeared to be relatively uniform.

The surface composition was further investigated by XPS analysis, as shown in Fig. 2g–i. The Li 1s peak appeared at 56.9 eV, while the F 1s peak observed at 685.0 eV was attributed to LiF. A Li 1s peak was observed at 55.3 eV, while Zn 2p doublet peaks were observed at 1043.6 and 1020.6 eV, indicating the presence of LiZn alloys on the foil. Additionally, due to surface oxidation, peaks arising from ZnO and Li_2O in the Li 1s and Zn 2p spectra could be detected.

While the oxidation layer of the Li metal surface is composed of fragile Li_2O and LiOH, which are unable to resist corrosion by H_2O and O_2, the ZnO and LiF components on the LiF@LiZn10/Li can protect the underlying Li from continuous oxidation.[38–40] As a result, the air stability of LiF@LiZn10/Li is significantly improved. Fig. 2j shows the visual change of pure Li and LiF@LiZn10/Li during exposure to the 20 RH% atmosphere. It was obvious that the pure Li was severely corroded and after 140 h exposure, whereby the surface of Li demonstrated a dark black color, indicating a complete oxidation of the surface. However, with the protection of surficial ZnO and LiF, LiF@LiZn10/Li retained a metallic luster after 36 h exposure. Even after 140 h exposure, the surface oxidation was weak and the foil appeared grayish. Meanwhile, both electrodes were also tested in a dry chamber with a 10% relative humidity, and as can be seen in Fig. S7† the same results were obtained. The improved air stability of LiF@LiZn10/Li would reduce the moisture control requirement for the manufacturing of LMBs, which could lower the cost of LMB assembly.

The LiF@LiZn10/Li electrode exhibits a practical capacity of about 10.37 mA h (Fig. S8†). Meanwhile, the specific capacity of the LiF@LiZn10/Li electrode was slightly decreased, measuring around 3263 mA h g^{-1} (Fig. S8†). Excluding the influence of surface oxidation, the test results were in good agreement with the theoretical calculations in Fig. S9 and Table S1.†

Symmetrical cells were constructed to assess the electrochemical performance of the LiF@LiZn10/Li foil electrode utilized in an ether electrolyte. The thickness of the LiF@LiZn10/Li foil was maintained at approximately 50 μm. As depicted in Fig. 3a, the LiF@LiZn10/Li‖LiF@LiZn10/Li cell

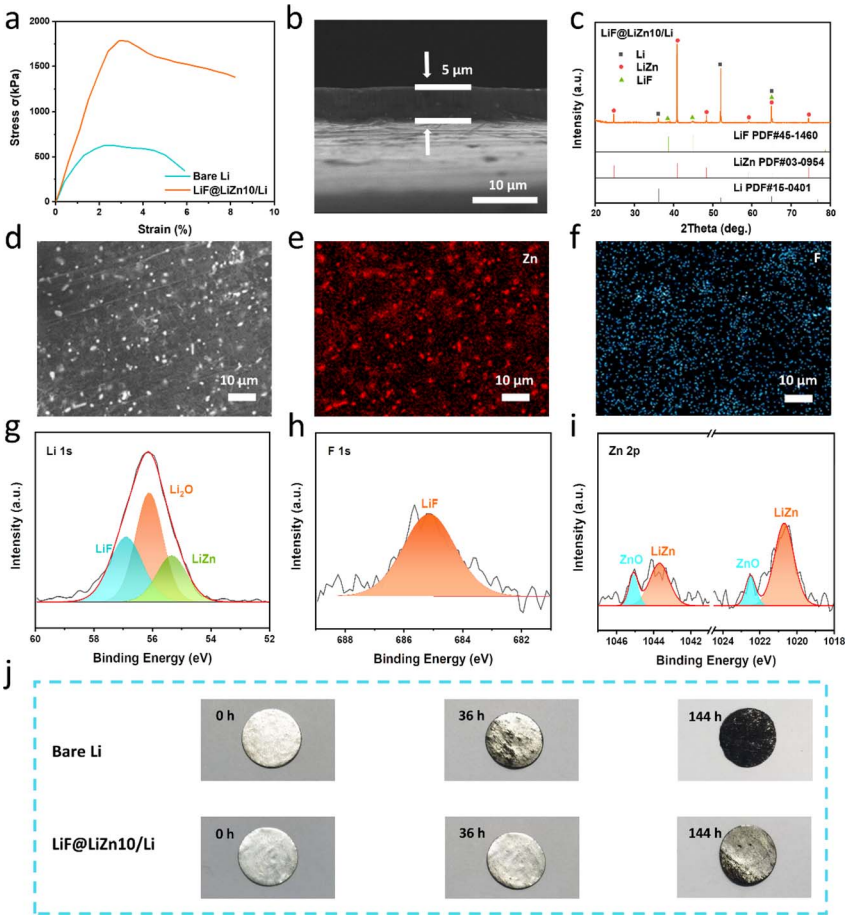

Fig. 2 (a) Tensile stress deformation curves of bare Li and LiF@LiZn10/Li foil. (b) SEM images of the LiF@LiZn10/Li foils with 5 μm thickness. (c) XRD patterns of the LiF@LiZn10/Li foil. (d–f) SEM and EDS images displaying the distribution of the Zn element and F element on the surface of the LiF@LiZn10/Li foil. (g–i) High-resolution XPS spectra of the Li 1s, F 1s, and Zn 2p of LiF@LiZn10/Li foil. (j) Surfaces of the bare Li electrode and LiF@LiZn10/Li electrode exposed in a controlled environment with a relative humidity (RH) of 20%.

exhibited a cycling duration of approximately 1300 h under the conditions of 1 mA cm^{-2} and 1 mA h cm^{-2}. In contrast, the Li||Li cell could only cycle for 700 h. When the current density was increased to 3 mA cm^{-2} and the capacity reached 3 mA h cm^{-2}, as shown in Fig. 3b both the LiF@LiZn10/Li and the bare Li electrodes experienced a substantial decrease in cycle life, consistent with the phenomenon of rapid lithium dendrite growth at high current densities. However, the LiF@LiZn10/Li electrode exhibited a cycle life of approximately 500 h, whereas the bare Li electrode could only endure for 260 h. Under the test conditions with 20% or even 40% depth of discharge (DOD) in Fig. S10,† the LiF@LiZn10/Li symmetric cell demonstrated good cycling performance. The presence of the lithiophilic element Zn contributed to a significantly lower polarization overpotential of the LiF@LiZn10/Li electrode compared to the bare Li electrode, as illustrated in Fig. 3c. Moreover, due to the stable interface between LiF@LiZn10/Li and the electrolyte, the polarization voltage of the LiF@LiZn10/Li foil electrode tended to stabilize as cycling progressed. Conversely, the SEI on the Li anode's surface was continuously destroyed and reconstructed, resulting in a continuous increase in polarization overpotential. Furthermore, the performances of the bare Li electrode and the LiF@LiZn10/Li foil electrode were evaluated using a commercial carbonate ester electrolyte. The LiF@LiZn10/Li foil electrode demonstrated more stable electrochemical cycling than the bare Li electrode (Fig. S11†), concurrently exhibiting a lower deposition potential.

The lower polarization and longer stable cycling life of the LiF@LiZn10/Li foil could be supported by the higher exchange current density. The exchange current density of the LiF@LiZn10/Li foil electrode was determined through Tafel testing. As depicted in Fig. 3d, the exchange current density of the LiF@LiZn10/Li foil electrode was measured at 0.037 mA cm^{-2}, which was higher than the 0.022 mA cm^{-2} observed for the bare Li electrode. This indicates that the LiF@LiZn10/Li foil electrode exhibited considerably faster charge transfer and improved electrochemical reaction kinetics. To validate the significant impact of the LiF@LiZn10/Li foil in enhancing the reaction kinetics of the electrode, EIS tests were conducted on both the LiF@LiZn10/Li||LiF@LiZn10/Li cell and the Li||Li cell. The charge-transfer resistance (R_{ct}) and solid-electrolyte interface resistance (R_{SEI}) of the LiF@LiZn10/Li||LiF@LiZn10/Li cell exhibited a gradual reduction during cycling, which aligned

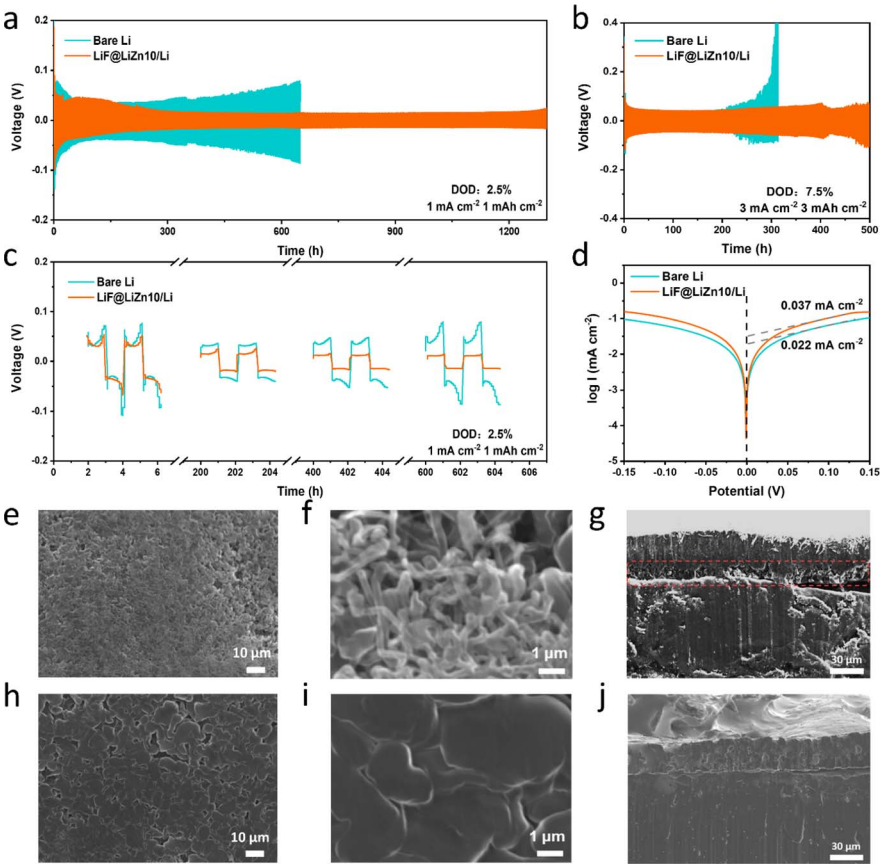

Fig. 3 (a and c) Cycling performance of bare Li and LiF@LiZn10/Li symmetric cells at 1 mA cm^{-2} and 1 mA h cm^{-2}. (b) Cycling performance of bare Li and LiF@LiZn10/Li symmetric cells at 3 mA cm^{-2} and 3 mA h cm^{-2}. (d) Tafel plots of bare Li and LiF@LiZn10/Li symmetric cells. (e, f and g) SEM images of the morphology after Li plating on the bare Li electrode at 6 mA h cm^{-2}. (h, i and j) SEM images of the morphology after Li plating on the LiF@LiZn10/Li electrode at 6 mA h cm^{-2}.

with the observed decrease in polarization shown in Fig. S12a.† Furthermore, after 100 cycles of 1 mA cm^{-2} and 1 mA h cm^{-2}, the symmetrical cell with the LiF@LiZn10/Li electrode demonstrated lower R_{ct} and R_{SEI} values compared to the Li||Li cell (Fig. S12b†). This reduction could be attributed to the presence of LiZn alloys and LiF particles in the LiF@LiZn10/Li foil electrode, which contributed to the improvement in the reaction kinetics.

The excellent electrochemical performance of the LiF@LiZn10/Li foil could be attributed to significantly improved Li deposition behavior on its surface. The surface morphologies of the bare Li and the LiF@LiZn10/Li foil after Li deposition of 6 mA h cm^{-2} at 1 mA cm^{-2} were characterized using SEM. As displayed in Fig. 3e and f, the surface of bare Li after Li deposition demonstrated a porous and loosely arranged structure. Upon closer examination, it was evident that Li deposition predominantly manifested in dendritic forms. These dendrites exhibited a high aspect ratio, with lengths exceeding 5 μm and diameters of approximately 100 nm. In contrast, the LiF@LiZn10/Li surface after deposition displayed a lower porosity, resulting in a smoother and denser surface, as shown in Fig. 3h and i. Fig. 3i reveals that the Li deposition was uniformly distributed and primarily in the form of blocks and rods. As shown in Fig. 3g, the thickness of the Li deposition reached approximately 44–48 μm. During Li deposition on the lithium metal surface, voids appeared, causing a volume expansion of the deposition layer. In contrast, Fig. 3j shows that the deposited Li on the LiF@LiZn10/Li surface was more uniform and dense, and the thickness of the deposition layer was noticeably reduced and similar to the theoretical thickness of approximately 33 μm. Meanwhile, the *in situ* optical microscopy images also clearly demonstrate that the LiF@LiZn10/Li electrode facilitates the uniform Li deposition behavior in Fig. S13.† These observations indicate that the LiF@LiZn10/Li electrode enables homogeneous Li diffusion, promotes uniform Li deposition, and effectively suppresses the formation of Li dendrites.

The improved Li deposition behavior could be attributed to the presence of LiZn alloys and LiF particles on the surface of the LiF@LiZn10/Li foil electrode. The heterogeneous lithium nucleation was the source of the formation of lithium dendrites. The naturally-formed fragile SEI fails to effectively restrain the growth of these dendrites. Nevertheless, the LiZn alloys present on the surface of the LiF@LiZn10/Li foil effectively offer uniform nucleation sites, reducing the nucleation overpotential of Li deposition and promoting the even deposition of Li^+

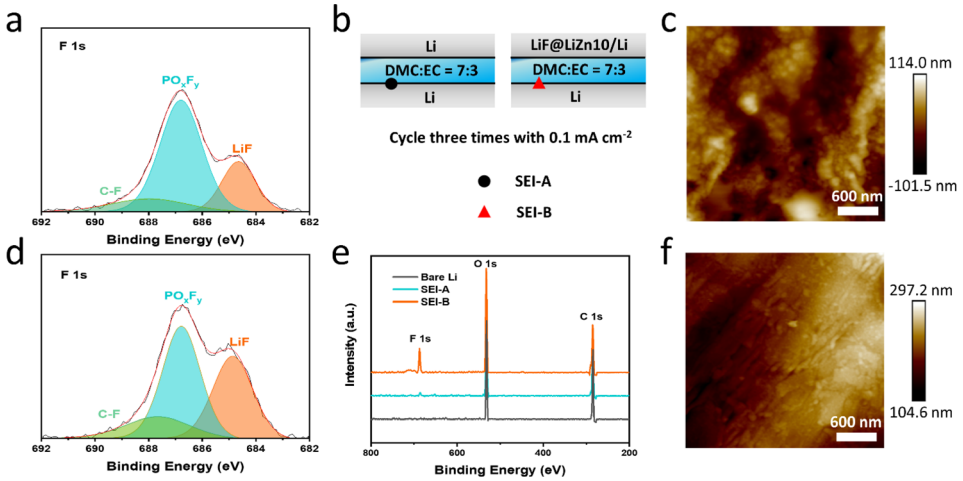

Fig. 4 (a) High-resolution XPS spectra of F 1s on the electrode surface of bare Li symmetric cell after 5 cycles. (b) Illustrations of the Li||Li symmetric cell (left) and the Li||LiF@LiZn10/Li symmetric cell (right). (c) AFM image of the SEI morphology on the bare Li surface. (d) High-resolution XPS spectra of F 1s on the electrode surface of the LiF@LiZn10/Li symmetric cells after 5 cycles. (e) XPS survey spectra obtained for bare Li, SEI-A, and SEI-B. (f) AFM images of the SEI morphology on the LiF@LiZn10/Li surface.

during the whole cycle life. Concurrently, compared to Fig. 4a and d, the content of LiF increased significantly in the SEI of the LiF@LiZn10/Li foil electrode after five cycles, as observed through XPS analysis. This was due to a surface of the LiF@LiZn10/Li foil and LiF-rich particles. The LiF component facilitates the formation of an SEI rich in LiF during the deposition process. This LiF-rich SEI alters the distribution of Li flux at the interface, leading to the formation of short and wide Li deposition morphologies instead of slender and elongated dendritic structures. Additionally, we speculate that the *in situ* regulation of LiF in the formation of the SEI on the lithium anode is a continuous process throughout the electrochemical cycling life.

To verify the working mechanism of LiF in the LiF@LiZn10/Li foil electrode during cycling, Li||Li and Li||LiF@LiZn10/Li cells with DME : EC (without $LiPF_6$) were assembled, as indicated in Fig. 4b. XPS was performed to obtain the surface composition of the Li electrode in the Li||Li cell (SEI-A) and Li||LiF@LiZn10/Li (SEI-B) after three cycles at 0.1 mA cm^{-2}. The surface of Li foil without electrolyte immersing and cycling was also analyzed for comparison. The survey XPS spectra showed the presence of F, O, and C signals at the SEI-A and SEI-B, as shown in Fig. 4e. The intensity of the F 1s signals at SEI-B was significantly stronger than that at SEI-A and bare Li. Subsequently, a semi-quantitative analysis of the elemental contents of F and O at different locations was conducted (Fig. S14†). The F content at SEI-B was nearly five times higher than that at SEI-A, while the O content at SEI-B was comparable to that at SEI-A. Considering that the electrolyte was free of the F element, the increased intensity of the F 1s signals at SEI-B arose from the counter LiF@LiZn10/Li foil electrode. Specifically, the LiF in the LiF@LiZn10/Li electrode dissolved in the solvent electrolyte during cycling, and participated in the formation of the SEI layer on the counter electrode (Li). As a result, a rich LiF-based SEI film was formed on the bare Li electrode in the Li||LiF@LiZn10/Li cell. It is worth mentioning that the F content of SEI-A was slightly higher than that of the bare Li electrode, suggesting that the F element was enriched on the electrode surface after cycling. Therefore, it could be concluded that LiF from the LiF@LiZn10/Li foil electrode can dissolve into the electrolyte, redistribute locally on the anode surface, and participate in the formation of the SEI, forming a LiF-rich interface layer during the cycling.[41] During cycling, the content of LiF in the SEI continuously increased (Fig. S15†). The deposition and dissolution of Li^+ and lithium metal in the LiF@LiZn10/Li electrode continuously expose LiF particles in the matrix to the electrolyte. Simultaneously, the dissolution mechanism of LiF particles ensures a continuous supply of LiF particles into the electrolyte, and together with the Li deposition, it participates in the formation of the SEI. This process enables the formation of an SEI rich in LiF during cycling. AFM tests of the electrodes were conducted after three cycles at 1 mA cm^{-2} and 1 mA h cm^{-2}. Fig. 4c reveals a rough SEI film formed on the bare lithium surface, characterized by numerous pits and an uneven texture. In contrast, Fig. 4f shows that the SEI film on the LiF@LiZn10/Li electrode exhibits a remarkably smooth and uniform surface with low roughness. Furthermore, we evaluated the mechanical properties of the SEI using the Derjaguin–Müller–Toporov (DMT) modulus. The SEI formed on the LiF@LiZn10/Li surface exhibited a higher average DMT modulus of 4.08 GPa, compared to 2.53 GPa for the SEI on the bare Li surface. The AFM results suggest that the LiF@LiZn10/Li electrode improved the Li deposition morphology, enhanced the mechanical strength of the SEI, and optimized its physicochemical properties during cycling. The LiF-rich SEI effectively enhanced Li^+ interface transport, suppressed lithium dendrite growth, and promoted a more uniform and stable electrochemical behavior of Li^+ on the surface of the lithium metal anode.[42] Additionally, the incorporation of LiF improved the stability of the SEI, effectively reducing the consumption of

lithium metal, mitigating electrolyte consumption, and significantly enhancing the overall stability and cycle life of the cells.[43,44]

To evaluate the potential application of the LiF@LiZn10/Li foil electrode in full cells, commercial $LiFePO_4$ cathodes (3.3 mA h cm^{-2}) were coupled with the as-prepared LiF@LiZn10/Li composite electrodes (50 μm). As illustrated in Fig. 5a, the $LiFePO_4$||LiF@LiZn10/Li cell with a practical N/P ratio of 2.59 exhibited superior cycling performance over 180 cycles, maintaining a steady CE of over 98% at 0.5C. In contrast, the $LiFePO_4$||bare Li cell exhibited rapid capacity decay after 50 cycles, accompanied by a lower and fluctuating CE, as shown in Fig. 5a. Moreover, by pairing with an ultrathin LiF@LiZn10/Li composite electrode (20 μm), a full cell with a practical N/P ratio of 1.04 was further constructed and investigated. Despite the limited amount of Li, the cell still offered stable cycling over 30 cycles with a capacity retention of 94% at 0.5C in Fig. S16.†

Fig. 5b illustrates that the $LiFePO_4$||LiF@LiZn10/Li full cell exhibited superior rate performance, particularly at high current rates. Notably, the $LiFePO_4$||LiF@LiZn10/Li full cell demonstrated reversible capacities of 140.8 mA h g^{-1} at 1C and 131.2 mA h g^{-1} at 1.5C, surpassing the capacities of 135.1 mA h g^{-1} and 82.8 mA h g^{-1} at 1C and 1.5C, respectively, for the $LiFePO_4$||bare Li cell (Fig. 5c and d). Its CE is included in Fig. S17.† This enhanced rate performance could be attributed to the rapid transfer of Li^+ ions at the interfaces and improved Li plating and stripping kinetics, leading to a reduction in the polarization potential during the electrochemical cycling of the LiF@LiZn10/Li electrode.

Furthermore, a pouch cell was constructed to assess the practical application potential of the LiF@LiZn10/Li electrode (Fig. S18†). As depicted in Fig. S18,† the pouch cell utilized NCM811 as the positive electrode material, a 40 μm-thick LiF@LiZn10/Li foil as the negative electrode, and a 3.18 g A h^{-1} injection ratio (Table S2†). The initial discharge capacity of the cell reached 130.2 mA h at 0.1C, corresponding to a high energy density of 350 W h kg^{-1}. The pouch cell exhibited excellent cycling performance, maintaining over 80% of its capacity after 80 cycles at 0.1C (Fig. 5e and f), accompanied by a CE of over 99.1% during the initial 50 cycles (Fig. S19†). This could be attributed to the formation of a LiF-rich SEI and the uniform deposition of lithium on the surface of the LiF@LiZn10/Li foil electrode during cycling. Additionally, SEM images of the LiF@LiZn10/Li electrode after cell cycling revealed smooth and dense Li deposition on the surface (Fig. S20a and b†). It is worth mentioning that the carbonate ester electrolyte ensured stable cycling of the pouch cell below 4.3 V (Fig. S21†). These results indicate that the LiF@LiZn10/Li foil exhibited exceptional electrochemical performance, offering valuable insights for the utilization of lithium metal in batteries with high energy density and long cycle life.

Conclusions

In conclusion, we propose a LiF@LiZn10/Li foil electrode with ultrathin lithium. This anode material was formed by the *in situ* formation of a LiZn alloy and LiF nanoparticles composite with lithium metal. The homogeneously dispersed LiZn alloys and LiF particles contributed to secondary strengthening, thereby significantly improving the mechanical properties and stability of the anode materials in ambient air. The LiF@LiZn10/Li foil could be prepared with a thickness of 5–50 μm lithium foil. Furthermore, the LiZn alloys and LiF particles embedded in the electrode enhanced the Li^+-diffusion kinetics. During the whole electrochemical cycling life, the presence of the LiZn alloys provides uniform nucleation sites for Li deposition, while the LiF particles dissolve into the electrolyte and participate in the formation of SEI, which enhances the cyclic stability of the electrode and improves the cycling performance of the batteries. The results show that the LiF@LiZn10/Li foil

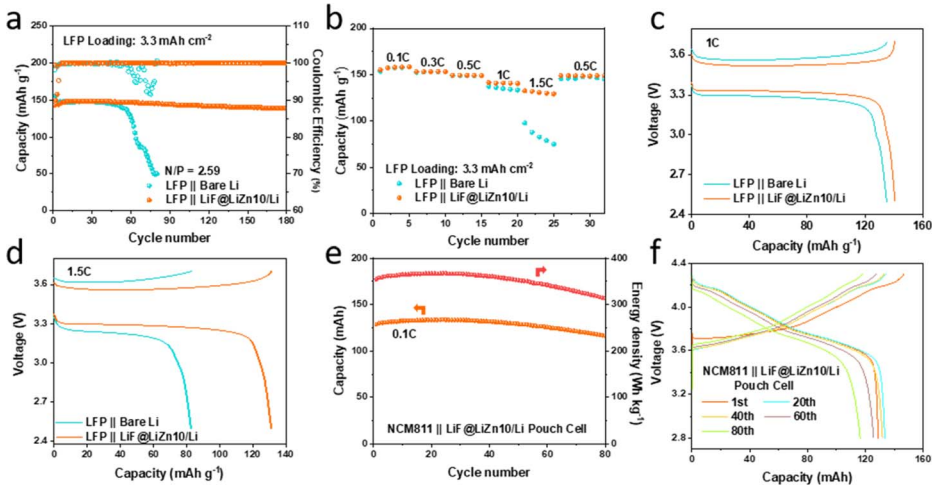

Fig. 5 (a) Cycling performance of $LiFePO_4$||bare Li and $LiFePO_4$||LiF@LiZn10/Li full cells at 0.5C. (b) Rate capability of $LiFePO_4$||bare Li and $LiFePO_4$||LiF@LiZn10/Li full cells. (c and d) Corresponding voltage profiles of $LiFePO_4$||bare Li and $LiFePO_4$||LiF@LiZn10/Li full cells at 1C and 1.5C. (e) Cycling performance of the NCM811||LiF@LiZn10/Li pouch cell. (f) Corresponding voltage profiles of the NCM811||LiF@LiZn10/Li pouch cell at different cycles.

electrode exhibited long-term and stable cycle stability in symmetrical cells and full cells. In addition, the high energy density (350 W h kg^{-1}) prepared by the LiF@LiZn10/Li foil electrode showed good cycling performance. Finally, this work proposes an *in situ* structural regulation strategy that addresses the non-uniform nucleation and interface design of lithium composite anodes, providing a pathway for the development of ultrathin Li metal anodes to achieve high energy density and long cycle life in batteries.

Author contributions

Jing Tao: investigation, methodology, formal analysis, writing-original draft. Can Zhang: writing-review & editing, software. Xueyang Li: writing-review & editing, methodology. Xinlong Chen: investigation, formal analysis. Chenzhen Ji: resources, funding acquisition. Wang Wan: resources, supervision, project administration. Chao Wang: writing-review & editing, methodology, supervision.

Conflicts of interest

There are no conflicts to declare.

Acknowledgements

This work was supported by the National Key Research and Development Program of China (2022YFB3803400), the Shanghai Pujiang Program (22PJ1413400), and the Fundamental Research Funds for Central Universities. The authors gratefully acknowledge the financial support from National Engineering Research Center of New Energy Vehicles, and Power Systems and Shanghai Key Lab of Vehicle Aerodynamics and Vehicle Thermal Management Systems.

Notes and references

1 B. Liu, J.-G. Zhang and W. Xu, *Joule*, 2018, **2**, 833–845.
2 W. Xu, J. Wang, F. Ding, X. Chen, E. Nasybulin, Y. Zhang and J.-G. Zhang, *Energy Environ. Sci.*, 2014, **7**, 513–537.
3 P. Bai, J. Li, F. R. Brushett and M. Z. Bazant, *Energy Environ. Sci.*, 2016, **9**, 3221–3229.
4 H. Zhang, Y. Yang, D. Ren, L. Wang and X. He, *Energy Storage Mater.*, 2020, **36**, 147–170.
5 C. Luo, H. Hu, T. Zhang, S. Wen, R. Wang, Y. An, S.-S. Chi, J. Wang, C. Wang, J. Chang, Z. Zheng and Y. Deng, *Adv. Mater.*, 2022, **34**, 2205677.
6 S. S. Zhang, *ACS Appl. Energy Mater.*, 2018, **1**, 910–920.
7 X. Xu, S. Wang, H. Wang, C. Hu, Y. Jin, J. Liu and H. Yan, *J. Energy Chem.*, 2018, **27**, 513–527.
8 C. Jin, T. Liu, O. Sheng, M. Li, T. Liu, Y. Yuan, J. Nai, Z. Ju, W. Zhang, Y. Liu, Y. Wang, Z. Lin, J. Lu and X. Tao, *Nat. Energy*, 2021, **6**, 378–387.
9 K.-H. Chen, K. N. Wood, E. Kazyak, W. S. LePage, A. L. Davis, A. J. Sanchez and N. P. Dasgupta, *J. Mater. Chem. A*, 2017, **5**, 11671–11681.
10 C.-J. Huang, B. Thirumalraj, H.-C. Tao, K. N. Shitaw, H. Sutiono, T. T. Hagos, T. T. Beyene, L.-M. Kuo, C.-C. Wang, S.-H. Wu, W.-N. Su and B. J. Hwang, *Nat. Commun.*, 2021, **12**, 1452.
11 S. J. Yang, F. N. Jiang, J. K. Hu, H. Yuan, X. B. Cheng, S. Kaskel, Q. Zhang and J. Q. Huang, *Electron*, 2023, **1**, e8.
12 Z. Su, J. Zhang, J. Jin, S. Yang and G. Li, *Chem. Eng. J.*, 2022, **430**, 132865.
13 A. Jana, S. I. Woo, K. S. N. Vikrant and R. E. García, *Energy Environ. Sci.*, 2019, **12**, 3595–3607.
14 R. Zhang, X. Chen, X. Shen, X.-Q. Zhang, X.-R. Chen, X.-B. Cheng, C. Yan, C.-Z. Zhao and Q. Zhang, *Joule*, 2018, **2**, 764–777.
15 X. Wang, Y. He, S. Tu, L. Fu, Z. Chen, S. Liu, Z. Cai, L. Wang, X. He and Y. Sun, *Energy Storage Mater.*, 2022, **49**, 135–143.
16 J.-F. Ding, Y.-T. Zhang, R. Xu, R. Zhang, Y. Xiao, S. Zhang, C.-X. Bi, C. Tang, R. Xiang, H. S. Park, Q. Zhang and J.-Q. Huang, *Green Energy Environ.*, 2023, **8**, 1509–1530.
17 Z. Zhang, Y. Jin, Y. Zhao, J. Xu, B. Sun, K. Liu, H. Lu, N. Lv, Z. Dang and H. Wu, *Nano Res.*, 2021, **14**, 3999–4005.
18 J. Cao, Y. Shi, A. Gao, G. Du, M. Dilxat, Y. Zhang, M. Cai, G. Qian, X. Lu, F. Xie, Y. Sun and X. Lu, *Nat. Commun.*, 2024, **15**, 1354.
19 S. Liu, J. Zhao, F. Li, Y. Zhao and G. Li, *J. Mater. Chem. A*, 2022, **10**, 5221–5229.
20 S. Han, Z. Li, Y. Zhang, D. Lei and C. Wang, *Energy Storage Mater.*, 2022, **48**, 384–392.
21 C. Li, S. Tu, X. Ai, S. Gui, Z. Chen, W. Wang, X. Liu, Y. Tan, H. Yang and Y. Sun, *Energy Environ. Mater.*, 2023, **6**, e12267.
22 K. Yan, Z. Lu, H.-W. Lee, F. Xiong, P.-C. Hsu, Y. Li, J. Zhao, S. Chu and Y. Cui, *Nat. Energy*, 2016, **1**, 16010.
23 C. Sun, A. Lin, W. Li, J. Jin, Y. Sun, J. Yang and Z. Wen, *Adv. Energy Mater.*, 2020, **10**, 1902989.
24 Y. Cheng, R. Lu, K. Amin, B. Zhang, Q. Zhou, C. Li, L. Mao, Z. Zhang, X. Lu and Z. Wei, *ACS Appl. Energy Mater.*, 2021, **4**, 6106–6115.
25 E. Peled and S. Menkin, *J. Electrochem. Soc.*, 2017, **164**, A1703–A1719.
26 Y. Gu, E.-M. You, J.-D. Lin, J.-H. Wang, S.-H. Luo, R.-Y. Zhou, C.-J. Zhang, J.-L. Yao, H.-Y. Li, G. Li, W.-W. Wang, Y. Qiao, J.-W. Yan, D.-Y. Wu, G.-K. Liu, L. Zhang, J.-F. Li, R. Xu, Z.-Q. Tian, Y. Cui and B.-W. Mao, *Nat. Commun.*, 2023, **14**, 3536.
27 H. Wu, H. Jia, C. Wang, J. G. Zhang and W. Xu, *Adv. Energy Mater.*, 2020, **11**, 2003092.
28 Y. Li, W. Huang, Y. Li, A. Pei, D. T. Boyle and Y. Cui, *Joule*, 2018, **2**, 2167–2177.
29 Z. Li, Y. Chen, X. Yun, P. Gao, C. Zheng and P. Xiao, *Adv. Funct. Mater.*, 2023, **33**, 2300502.
30 Y. Guo, S. Pan, X. Yi, S. Chi, X. Yin, C. Geng, Q. Yin, Q. Zhan, Z. Zhao, F. M. Jin, H. Fang, Y. B. He, F. Kang, S. Wu and Q. H. Yang, *Adv. Mater.*, 2023, **36**, 2308493.
31 X. Y. Yue, Y. X. Yao, J. Zhang, S. Y. Yang, Z. Li, C. Yan and Q. Zhang, *Adv. Mater.*, 2022, **34**, 2110337.
32 W. Wu, W. Luo and Y. Huang, *Chem. Soc. Rev.*, 2023, **52**, 2553–2572.

33 A. Masias, N. Felten, R. Garcia-Mendez, J. Wolfenstine and J. Sakamoto, *J. Mater. Sci.*, 2019, **54**, 2585–2600.
34 C. Zhang, H. Fan, X. Chen, H. Xu, J. Lou, Y. Li, Y. Huang and S. Li, *Energy Environ. Sci.*, 2022, **15**, 5251–5260.
35 Z. Guo, T. Wang, D. Wang, H. Xu, X. Liu, Y. Dai, H. Yang, Y. Huang and W. Luo, *ACS Nano*, 2023, **17**, 14136–14143.
36 J. Gao, C. Chen, Q. Dong, J. Dai, Y. Yao, T. Li, A. Rundlett, R. Wang, C. Wang and L. Hu, *Adv. Mater.*, 2021, **33**, 2005305.
37 J. Zhang, X. Yue, Z. Wu, Y. Chen, Y. Bai, K. Sun, Z. Wang and Z. Liang, *Nano Lett.*, 2023, **23**, 9609–9617.
38 J. Wu, L. Yuan, Z. Li, X. Xie and Y. Huang, *Mater. Horiz.*, 2020, **7**, 2619–2634.
39 D. Lin, Y. Liu, W. Chen, G. Zhou, K. Liu, B. Dunn and Y. Cui, *Nano Lett.*, 2017, **17**, 3731–3737.
40 H. Li, F. Zhang, W. Wei, X. Zhao, H. Dong, C. Yan, H. Jiang, Y. Sang, H. Chen, H. Liu and S. Wang, *Adv. Energy Mater.*, 2023, **13**, 2301023.
41 G. Li, X. Duan, X. Liu, R. Zhan, X. Wang, J. Du, Z. Chen, Y. Li, Z. Cai, Y. Shen and Y. Sun, *Adv. Mater.*, 2022, **35**, 2207310.
42 A. Ramasubramanian, V. Yurkiv, T. Foroozan, M. Ragone, R. Shahbazian-Yassar and F. Mashayek, *J. Phys. Chem. C*, 2019, **123**, 10237–10245.
43 J. Tan, J. Matz, P. Dong, J. Shen and M. Ye, *Adv. Energy Mater.*, 2021, **11**, 2100046.
44 Q.-K. Zhang, X.-Q. Zhang, J. Wan, N. Yao, T.-L. Song, J. Xie, L.-P. Hou, M.-Y. Zhou, X. Chen, B.-Q. Li, R. Wen, H.-J. Peng, Q. Zhang and J.-Q. Huang, *Nat. Energy*, 2023, **8**, 725–735.